SUPPORTING INFORMATION

Artificial cytoskeleton shells supported on giant vesicles

Iván López-Montero, Ruddi Rodríguez-García and Francisco Monroy

Mechanics of Biological Systems and Department of Physical Chemistry I, Universidad Complutense, 28040 Madrid (Spain)
E-mail: (monroy@quim.ucm.es; ivanlopez@quim.ucm.es)

1. MATERIALS AND SPECIFIC METHODS

Chemicals. Sodium Chloride (NaCl), Potassium chloride (KCl, 99.5%), sodium phosphate (NaH_2PO_4), Magnesium sulphate ($MgSO_4$), Magnesium Chloride ($MgCl_2$), Ethylenediaminetetraacetic acid (EDTA), Adenosine-5'-triphosphate (ATP) and Hepes were supplied by Sigma-Aldrich. Glucose and sucrose were from Riedel-de Haën. Ultrapure water was taken from a Milli-Q unit (Millipore, conductivity lower than 18MΩ cm, organic residuum less than 2ppb).

Lipids. The fluorescent probes 1,2-dioleoyl-*sn*-glycero-3-phosphoethanolamine-N-(lissamine rhodamine B sulfonyl) (Rh-PE), 1-oleoyl-2-{6-[(7-nitro-2-1,3-benzoxadiazol-4-yl)amino]hexanoyl}-*sn*-glycero-3-phosphocholine (NBD-PC), 1-oleoyl-2-{6-[(7-nitro-2-1,3-benzoxadiazol-4-yl)amino]hexanoyl}-*sn*-glycero-3-phosphoserine (ammonium salt) (NBD-PS) and N-[6-[(7-nitro-2-1,3-benzoxadiazol-4-yl)amino]hexanoyl]-sphingosine-1-phosphocholine (NBD-SM), were supplied by Avanti Polar Lipids. Lipids are dissolved in chloroform at 1mg/ml. Lipid solutions are stored at –20ºC.

Antibodies. Monoclonal anti-human spectrin (α and β) (clone SB-S1) was purchased from Sigma-Alrich. The secondary fluorescent antibody Alexa Fluor 488 goat anti-mouse IgG, IgA, IgM (H+L) was supplied by Invitrogen.

Erythroid membrane extract (EME). Human blood was obtained in fresh from healthy donors and stored in EDTA-containing tubes to avoid coagulation. Erythrocyte ghosts were prepared from extracted erythrocytes following the Steck and Kant protocol [1]with minor modifications described for enhancement of hemoglobin removal under hemolysis/resealing conditions[2]. The erythrocyte concentrate is obtained by washing out three times in PBS buffer (1 blood / 5 PBS (vol/vol); NaCl 150 mM, sodium phosphate 5 mM, pH = 8). Then, cytoplasm contents are removed under hemolytic conditions in a hypotonic buffer (1 erythroid extract / 40 buffer (vol/vol); 1mM $MgSO_4$, sodium phosphate 5 mM, pH = 8). Sealed ghosts were recuperated after centrifugation (22000g, 10 minutes; 4ºC). The hard button enriched in proteases obtained at the tube bottom was carefully removed. The buffer washing out was repeated twice again in a dilution ramp at constant pH = 8 (1st: 1mM $MgSO_4$, sodium phosphate 2.5 mM; 2nd: 1mM $MgSO_4$, sodium phosphate 1.25 mM). The procedure was carried out at 4ºC. The erythroid membrane extract (EME) is obtained at a final concentration *ca.* 5mg/ml (estimated). Then, EMEs were vesiculated by passing the extract suspension 5 times through a gauge needle (No. 23) using a 50 mL syringe. Aliquots (20 μL) of the RBC membrane concentrate were stored at −20ºC.

Spectrin/Ankyrin depletion from EME. Prior to vesiculation, membrane extracts were incubated for 30 minutes at 37ºC in low ionic strength buffer (EDTA 1 mM, Sodium phosphate 0.3 mM, pH = 8). After this first incubation spectrins are efficiently detached from the membranes, recuperating an insoluble membrane extract devoid of spectrin (EME Sp^-) after centrifugation (7000g, 30 minutes; 4ºC). Then, EME Sp^- was incubated again for 30 minutes at 37ºC in high ionic strength buffer (KCl 1M, EDTA 1 mM, sodium phosphate 5 mM, pH = 8). This process causes ankyrin detachment, obtaining a final extract devoid of spectrin and ankyrin (EME Sp^- Ank^-) after centrifugation (8000g, 30 minutes; 4ºC).

Analysis of cytoskeletal protein components by gel electrophoresis. Proteins were analyzed by sodium dodecyl sulfate (7%) polyacrylamide gel electrophoresis (SDS-PAGE)[3]. Figure S1 shows the running band obtained for the extract of erythrocyte membranes (EME) and revealed by coomassie brilliant blue. In this chromatogram, all the proteins composing the human RBC cytoskeleton were found. Particularly, we detect in EME (Fig. S1A) the membrane proteins α−,β−spectrin (at 240 and 220 kD,

respectively), ankyrin (visible as a weak line at 210kD), bands 3/4.1 (at 100 and 82 kD, respectively) and soluble actin (an intense line at 43kD). The analysis corresponding to EME Sp^{-} Ank^{-} (Fig. S1B) reveals effective extraction of the fibrilar proteins spectrin and actin and of the main membrane anchor ankyrin.

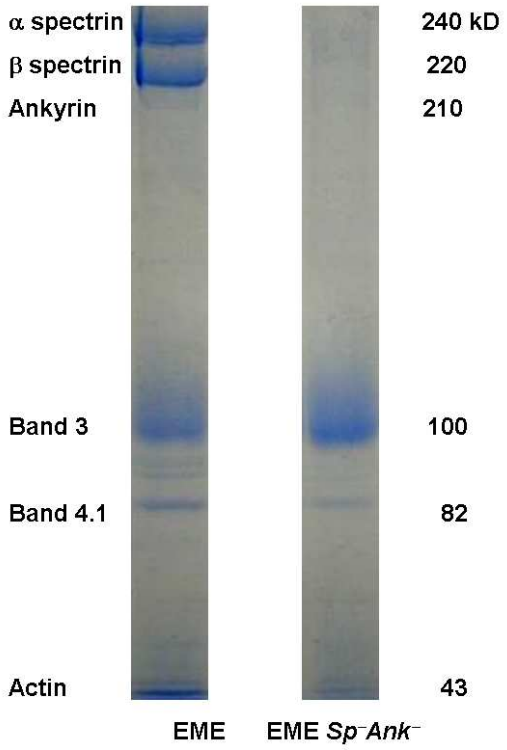

Figure S1. Chromatographic SDS-PAGE of the erythroid membrane extracts (EME) and EME devoid of spectrin and ankyrin (EME Sp^{-} Ank^{-}). These runs correspond to the membrane extracts used in this work.

Indirect inmunofluorescence. Freshly prepared erythGUVs were incubated for 1 hour in isosmolar buffer solution containing primary monoclonal anti-human α,β-spectrin (anti-body final concentration, 4 μg/ml, 75 mM NaCl, 40 mM glucose, 10 mM Hepes, 1mM $MgCl_2$, 1 mM KCl, pH = 7,4). The secondary fluorescent antibody Alexa Fluor 488 goat anti-mouse IgG, IgA, IgM (H+L) (*ca.* 4 μg/ml, final) was subsequently incubated for 1 hour more. When no ATP is present, erythGUVs appear as an homogeneous fluorescent corona corresponding to the specific location of spectrin at the membrane site (Fig. 1E). In the presence of ATP (2 mM), the homogeneous fluorescence rapidly clusters into filament structures forming the observed spectrin network (Fig. 1A-D).

Fluorescent labelling of membrane extract with lipid probes. To specifically identify lipid-spectrin interactions, prior to spreading on the electroformation chamber erythroid membranes were labelled with fluorescent lipid dyes. For that, EME aliquots were incubated for 30 minutes in an Eppendorf tube previously containing a lipid film. These films are prepared by solvent evaporation from a chloroform solution containing 1μg of the fluorescent probes (Rh-PE, NBD-PC, NBD-PS or NBD-SM).

2. GRAPH ANALYSIS

A. Skeletonization: branch length and node coordination.

The structure of a skeletal network can be rationalized from its underlying tree structure. A skeleton tree is formed by branches and junction nodes where three or more branches link together. In shape analysis, the topological skeleton of a given network represents the thinnest representation (one dimension) of the real thick structure. The skeleton usually emphasizes geometrical and topological properties of the shape, such as its coordination, connectivity, fractal dimension and order. Skeletonization algorithms compute the skeleton as lines equidistant to the boundaries of the thick object. We have developed a Matlab code first passing the real images through a binarization function (Matlab function: *im2bw*) and then by a skeletonization algorithm (*bwmorph*) which renders the 1D-topological representation of the original skeletal network as nodes and branches. Figure S2 shows a typical example case (S2A: original network; S2B: skeletonized image). Further, for a given node the coordination degree is defined as the number of branch connections it has to other nodes in the network. Figure S2C shows how the graphical algorithm *Analyse Skeleton* (a plug-in of ImageJ) discretizes the skeleton in Fig. 2B into nodes and branches (see caption for details).

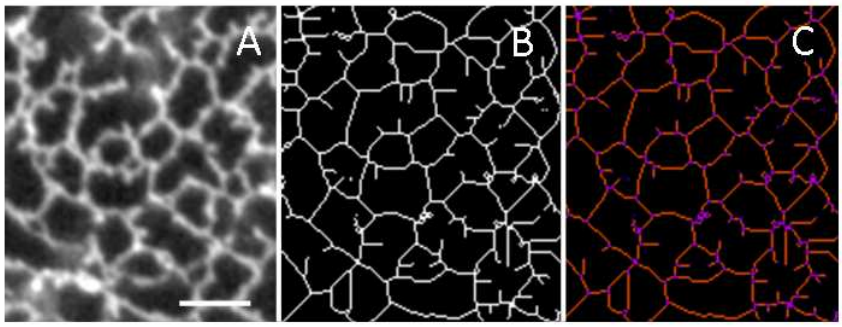

Figure S2. A) original network. Scale bar: 5μm; **B)** skeletonization of A); **C)** after counting algorithm *Analyse Skeleton* of Image J; branches in orange; nodes as pink pixels.

For a given skeleton, the statistical distribution of the branch lengths and the coordination of the nodes were determined using *Analyse Skeleton*. From a population of 28 different samples (see Fig. S3 for a representative gallery), the distributions of branch lengths, $a \approx 2.1$ (±0.5) μm and node coordination (3-fold 70%; 4-fold 20%; others 10%) were statistically determined (the quantities between parentheses represent the standard deviation).

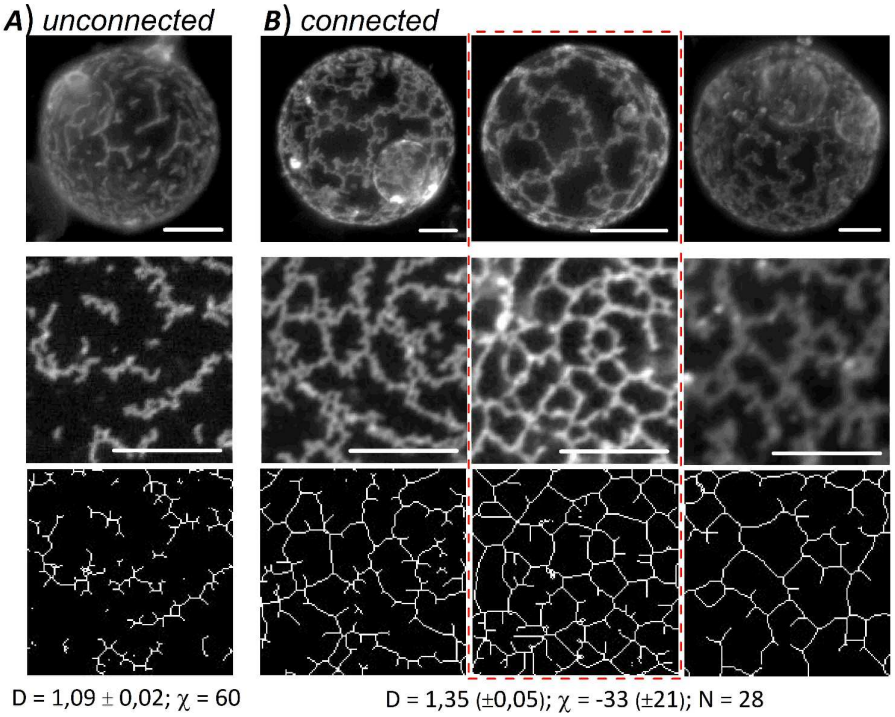

Figure S3. Image gallery of the different skeleton morphologies found in experiments (*top panel:* 3D-tomagraphies of the artificial erythroid vesicles; *medium:* planar fixations at slide bottoms; the white scale bars correspond to 10μm) and their respective skeletonization by ImageJ *(bottom panel).* ***A)*** Typical unconnected trees found at defective ATP. In this case, the system organizes as a number of individual trees with a low degree of ramification and a reduced interconnectivity, defined by a low fractal dimension $D = 1.09 \pm 0.02$ and a positive value of the Euler characteristic ($\chi >> 0$; see Section C). This constitutes an open structure predominantly made of *quasi*-1D filaments. ***B)*** Typical network skeletons formed in excess ATP. In these cases, extensive linking between the different trees entails high 2D-networking (the average fractal dimension $D = 1.35$ (±0.05), standard deviation; $N = 28$), thus resulting in a discrete number of connected objects with a higher degree of internal connectivity ($\chi << 0$) than isolated trees in *A).* The central panel (squared in red) represents the commonest topology based on relatively large filaments with low lateral grafting but high connectivity, thus resulting in closed network structures with a high degree of

reticulation (closed corrals). This can be considered the *more typical* network case found in experiments (Fig. 1 in the main text).

B. Dimensional analysis

The fractal dimension, D, is the topological characteristic that indicates how completely a graph appears to fill space[4]. For tree- and skeleton- graphs, the degree distribution is the probability distribution of the local density of coordination nodes calculated over the whole network (N_{nodes}). The degree distribution is a statistical quantity solely determined by the fractal dimension of the topological graph. If the degree distribution follows a power-law with the system size, the network is said scale-free, which implies a self-similar structure on all length scales:

$$N_{nodes} \sim L^{D} \qquad \text{(Eq. S1)}$$

where L represents a spatial length scale.

This class of fractal scaling is easily determined by the box counting method, which is a gridding method measuring the power-law relation existing between the size of the grid box and the number of boxes required to cover the object. First, the function *FracLac2.5* of ImageJ grids the skeleton into boxes of different size L. Then, the algorithm calculates the dependence between the linear size of the box (L) and the number of boxes needed to cover the network (M). A typical analysis case is shown in Figure S4, although this behavior is systematically found for the different skeletons observed experimentally. For a given skeleton graph, *FracLac2.5* performs a statistical analysis exploring length scales with a growing size above a lower cut-off fixed as the minimal box necessary for the graphical resolution of a node and the emerging branches (3×3 pixels square; 0.3μm length). An application case of the box counting method applied to a real skeleton is depicted in Fig. S4A. At small lengths ($L << a$; *grids1-2* in Fig. S4A-B), the tiny boxes cover just network elements but little space abroad (free space), thus giving an adequate measurement of the systemic topology of the network. At a crossover region ($L \approx a$; *grid3*), some boxes start to cover not only skeleton but also a significant fraction of free space. At larger box sizes ($L >> a$; *grid4*), each box touches several skeleton elements covering the free space around in a way such that the whole 2D-space is practically wrapped up by the box grid. The fractal dimension is measured as the power law exponent for the number (M) of boxes of linear size L

needed to cover the network (because M varies inversely with the average number of vertices within a box thus Eq. S1 rewrites as $M \sim L^{-D}$).

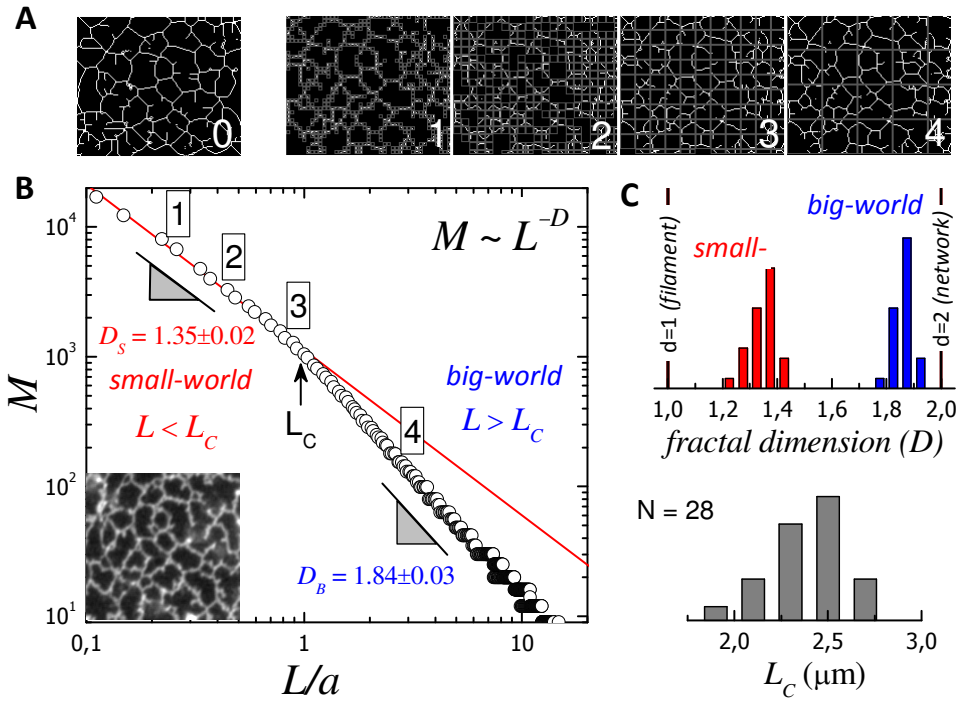

Figure S4. ***A)*** Fractal analysis of a typical spectrin skeleton (a = 2.5 ± 0.1 μm) (**0**: the same skeleton as in *B;* **1-4**: box-gridding at different spatial scales). By performing grids of size L, *FracLac2.5* (ImageJ) counts the number of boxes M needed to cover the network. The numbers indicate the location of the different counting boxes in *B).* ***B)*** Typical fractality *M-L* plot of the real skeleton in *A)* (characteristic mesh size a = 2.1 ± 0.2 μm). Two distinct self-similar regimes are clearly discernable: *small-world* filamentous sub-structure ($D_S \approx 1.35$ at $L/a < 1$); *big-world* network supra-structure ($D_S \approx 1.85$ at $L/a > 1$). ***C)*** Statistical analysis of the fractal dimension of the two regimes *(top panel)* and of the crossover length between them *(bottom panel)* performed over a population of 28 different skeleton networks.

At length scales smaller than the characteristic mesh size ($L < a$), the skeletal topology follows power-law behavior $M \sim L^{-D}$ with D_S = 1.35 (±0.10; standard deviation, N = 28; Fig. S4B), characteristic for a nearly one-dimensional self-similar graph at distances shorter than the filament length a. Actually, Figure S4 shows as in the *small-world* ($L < a$) the skeleton consists of a succession of linear contours with sporadic ramifications giving rise to a surface network with a fractionary fractal dimension. The nearer is D to the euclidean dimension (d = 2 for a membrane structure) the higher is space completion. Consequently, a panoramic view should provide the *big-world* description

as a network skeleton nearly filling the surface space in the membrane ($d = 2$), thus in the limit $L >> a$ one measures a fractal exponent close to spatial dimension, $D_B = 1.85$ (±0.05).

C. Connectivity analysis: Euler characteristic

The connectivity of skeleton networks is usually quantified by the Euler characteristic χ, a topological invariant describing the mesh shape regardless of the way it is bent[5, 6]. This characteristic is defined as the difference between the number of connected skeleton objects (N_{sk}) minus the number of connections (N_c) forming either open trees and closed corrals in the network ($\chi = N_{sk} - N_c$). A positive value unequivocally corresponds to high degree of network disconnection into weakly branched skeletons and predominantly opened structures. Conversely, a high network connectivity is characterised by a highly negative χ−value, indicating a sole (or a few) connected skeleton(s) defining a high number of enclosed corrals inside.

In the present work, the Euler connectivity was calculated using the skeletonization protocols in Section A (ImageJ), further passing the binarised images by a Matlab algorithm *(bmweuler)*[7] coded for counting connected objects and corrals. The Euler characteristic of the different skeleton structures systematically resulted in negative values corresponding to a low number of isolated skeletons with a high degree of connection inside. Typical values, calculated for individual skeletons are shown in Figure S3. A statistically average value of the Euler characteristic $\chi = -33$ (±21) is calculated over a population of 28 different connected skeletons.

D. Lacunarity

The lacunarity deals with the degree of gappiness, or visual homogeneity, of a connected structure[8]. For a network, the lacunarity parameter Λ is calculated as the standard deviation of the local density of empty space (*"lacunae"*) with respect to its average value. In practice, one counts black pixels inside boxes of different size L in a grid ($N_p^{(j)}$). Then, the standard deviation (δN_p) is referred to the average value calculated over the whole grid ($N_p = \sum_j N_p^{(j)}$). For each L, lacunarity is computed as[9]:

$$\Lambda(l) = 1 + \left(\frac{\delta N_P}{N_P} \right)^2 \qquad \text{(Eq. S2)}$$

Usually, lacunarity is considered a measure of the distribution of empty space in an image. For skeletal network, consequently Λ informs how homogenously is the space covered by the skeleton at different scales. If an image with fractal geometry displays high diversity of gap sizes and object shapes, lacunarity is high. Contrarily, if the fractal structure is homogeneously distributed across the space, the gap distribution is then invariant and the lacunarity converges to unity. An unitary lacunarity indicates structural homogeneity whilst $\Lambda > 1$ is indicative of non-uniformity. Based on the above definition, the present analysis was performed using a Matlab code[10].

Figure S5 plots the average results obtained as average values from a skeleton population (N = 28; error bars corresponds to the standard deviation over the different images). At small scales, the present skeleton graphs show relatively high lacunarity, as expected for a distorted structure with a non-uniform distributions of gaps ("lacunae")[11]. As larger scales are "zoomed" into the *big-world* (increasing the box size, L), distortions become uniformly distributed and lacunarity converges to a low value close to unity, $\Lambda \approx 1.004$, compatible with an homogenous distribution of the skeleton elements and the free space.

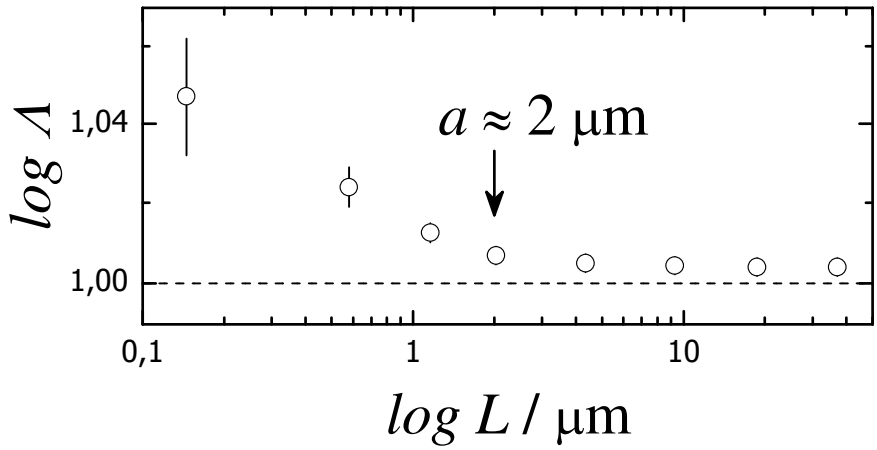

Figure S5. Lacunarity analysis of spectrin skeletons. The different images are square-sectioned in grids of size L. For a given skeleton, the parameter Λ is calculated as a function of L using Eq. S2. Each L-value is averaged over the population of 28 skeletons used in this work (the error bar is a standard deviation).

E. Order parameter

Disorder in a skeleton network is quantified by an order parameter S defined as[12]:

$$S = 2\left\langle \cos^2\left(\theta_i\right)\right\rangle - 1 \qquad \text{Eq. S3}$$

where θ_i measures the orientation of the *i*–branch with respect to an horizontal axis.

If $S = 0$, there is no preferred direction in average corresponding to an isotropic distribution. Conversely, $S = 1$ corresponds to a totally ordered structure with a preferential direction.

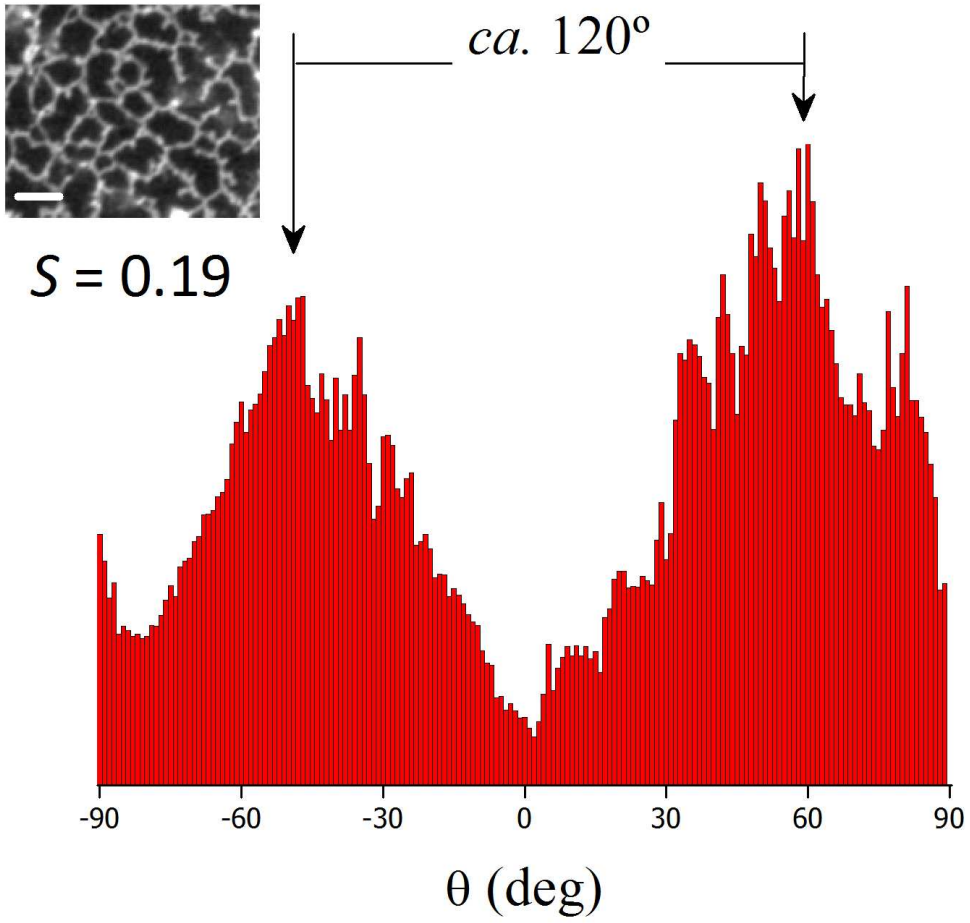

Figure S6. Typical orientation analysis of the spectrin skeleton shown in the figure (White line is 5μm. See text for details).

Figure S6 shows a distribution histogram of the orientational angles θ with respect to the horizontal axis as determined by *OrientationJ* (ImageJ) for a typical spectrin skeleton. A broad orientational distribution typical of a highly disordered network is reported in the present case. However, two sparse maxima are observed separated by *ca.* 120º, as expected from the predominant triangular coordination. Similar results are found for the other skeletons along our image repertoire, unequivocally, a proof of the high topological polydispersity of the present artificial networks.

3. FLUCTUATION ANALYSIS

A. Ultrafast flickering spectroscopy. In a typical flickering experiment, thermal fluctuations are tracked as local changes of the vesicle radius δR observed at the equatorial plane. In our set-up, fluctuating erythGUVs (sized typically $R \approx 10$ μm) are visualized using phase contrast microscopy (Nikon EclipseTi, oil-immersion objective 100×). The flickering dynamics is recorded by an ultrafast CMOS camera (Photron FastCAM SA3, 200 kfps maximum rate, 1 Mpixel)[13]. At optimal illumination, the acquisition rate was fixed at 5 kfps. Then, each vesicle profile is digitalised and the fluctuation function, $\delta R(x,t_i)$, obtained at each time with respect to the instantaneous circular radius R_0, calculated as the centre-of-mass of the circular contour. The deformation function $\delta R/R$ is expanded in series of discrete Fourier modes:

$$z = \frac{dR}{R} = \sum_q \left(a_q \sin qx + b_q \cos qx \right) \qquad \text{Eq. S4}$$

where $q(l) = l/R$ (with $l = 2, 3, 4, \ldots$).

The Fourier series is in practice truncated at $l \approx 50$, where the calculated amplitudes vanish below the experimental uncertainty. From the above mode decomposition, the fluctuation amplitudes are defined in the reciprocal space as:

$$z_q(t) = \pm \sqrt{a_q^2 + b_q^2} \qquad \text{Eq. S5}$$

where the sign + indicates the absolute value.

B. Amplitude spectrum. A comprehensive description of the reduction methods used to analyze the experimental shape fluctuations of GUV's can be found in the state-of-art work by Pécrèaux *et al.* [14]. The specific procedures used for the analysis of the fluctuation spectra were protocolised as Auxiliary Material in the previous Ref.[15]. Here, we just reproduce the more relevant aspects related to the q-dependence of the fluctuation spectrum measured at the equatorial plane. Experimentally, from the amplitudes in Eq. S5 one obtains the spectrum of the equatorial fluctuations as:

$$P_{eq}(q_x) = \left\langle z_q(t) z_q(t) \right\rangle \qquad \text{Eq. S6}$$

where the time average is calculated over a time series typically containing 5000 frames. Consequently one actually measures[14] ***(Error! Bookmark not defined.)***:

$$P_{eq}(q_x) = \frac{1}{2p}\int_{-\infty}^{\infty} P(\mathbf{q})dq_y \qquad \text{Eq. S7}$$

where $P(\mathbf{q})$ is the fluctuation spectrum of the radial fluctuations characterised by a wavevector $\mathbf{q} = (q_x, q_y)$. For fluid membranes one usually considers the classical Helfrich spectrum of the tension/bending modes[16]. When projected on the equatorial plane one gets:

$$P_{eq}(q_x) = \frac{1}{2p}\int_{-\infty}^{\infty} \frac{k_B T}{s q^2 + k q^4} dq_y \qquad \text{Eq. S8}$$

This ansatz can be expanded in simple fractions as:

$$\begin{aligned} P_{eq}(q_x) &= \frac{1}{2p}\int_{-\infty}^{\infty} \frac{k_B T}{s q^2 + k q^4} dq_y = \frac{1}{2p}\int_{-\infty}^{\infty} \frac{k_B T}{q^2\left(s + k q^2\right)} dq_y = \\ &= \frac{1}{2p}\int_{-\infty}^{\infty} \frac{k_B T}{s q^2} dq_y - \frac{1}{2p}\int_{-\infty}^{\infty} \frac{k}{s}\frac{k_B T}{s + k q^2} dq_y \end{aligned} \qquad \text{Eq. S9}$$

since $q^2 = q_x^2 + q_y^2$, direct integration over q_y leads to:

$$P_{eq}(q_x) = \frac{k_B T}{2s}\left[\frac{1}{q_x} - \frac{1}{\sqrt{(s/k) + q_x^2}}\right] \qquad \text{Eq. S10}$$

This expression leads to two limit behaviors for the curvature fluctuations: the *capillary-like* regime, $P_{cap} \approx k_B T/\sigma q_x$, found at low q ($< q_{cap} \approx (\sigma/\kappa)^{1/2}$) and high σ, and conversely, the *bending* regime well above q_{cap}, where curvature fluctuations show a dependence $P_{bend} \approx k_B T/\kappa q_x^3$, dominated by bending elasticity κ.

C. Shear contribution: effective lateral tension. The fixed connectivity provided by the skeleton network might entail solid-like character to the membrane where it is attached. Consequently, a finite shear component ($\mu > 0$) should emerge as an additional rigidity contribution to elastic modes. In the flat membrane, shear effects cause a renormalization of the bending constant to higher values at the microscopic limit of small wavevectors ($q \to 0$)[17, 18]. In this regime, the effective bending rigidity of the solid membrane is given by[17, 19-21]:

$$k_{eff}(\mathbf{q}) \gg k_0 + \sqrt{\frac{3\mu k_B T}{4p}}\mathbf{q}^{-1} \qquad \text{Eq. S11}$$

Consequently, the flexural modes of the undulating membrane are affected by the shear

term in Eq. S11 which introduces a q^{-3}-dependent contribution to the usual Helfrich spectrum; in the $q \to 0$ limit one has[19] ***(Error! Bookmark not defined.)***:

$$P(q) \approx \frac{k_B T}{\sigma q^2 + \sqrt{3\mu k_B T / 4\pi} q^3 + \kappa q^4} \qquad \text{Eq. S12}$$

For very rigid membranes ($\mu >> \sigma$) the shear mode dominates, thus the equatorial spectrum might be found to vary as:

$$P_{eq}(q_x \to 0) \approx \frac{1}{2\pi} \int_{-\infty}^{\infty} \frac{k_B T}{(3\mu k_B T / 4\pi)^{1/2} q^3} dq_y \approx \sqrt{\frac{4\pi k_B T}{3\mu}} \frac{1}{q_x^2} \qquad \text{Eq. S13}$$

which defines a renormalization from the usual $P_{eq}(q_x) \sim q_x^{-3}$ dependence of the bending modes to a $P(q_x \to 0) \sim q_x^{-2}$ regime, typical of shear modes.

In vesicles, the surface is curved thus the shear energy is already quadratic in the normal displacements, and it is not sensitive to the above renormalization effects[20] ***(Error! Bookmark not defined.)***. For rigid vesicles, a wavevectors above $q_C \approx (3\mu k_B T/4\pi)^{1/2} / \kappa$, theory predicts[18, 21] ***(Error! Bookmark not defined.,Error! Bookmark not defined.)***:

$$k_{eff}(\mathbf{q}) \approx k_0 + \frac{9\mu k_B T}{16\pi k_0} \mathbf{q}^{-2} \qquad \text{Eq. S14}$$

Consequently, for solid-like vesicles in the high q-regime, the shear term is expected to take the same quadratic dependence as the tension contribution, *i.e.* the spectrum of the curvature modes is expected in these cases to vary as the classical Helfrich spectrum:

$$P_{sk}(q) \approx \frac{k_B T}{\sigma_{sk}^{(eff)} q^2 + \kappa_{sk} q^4} \qquad \text{Eq. S15}$$

with $\kappa_{sk} > \kappa_0$ (due to structural stiffening) and the shear-dependent effective tension:

$$\sigma_{sk}^{(eff)} \approx \sigma_0 + \frac{9\mu k_B T}{16\pi k_0} \qquad \text{Eq. S16}$$

When the membrane skeleton is present, we can fit the experimental spectra to the equatorial projection of the Helfrich spectrum in Eq. S10, thus obtaining the effective values for the mechanical parameters (Eqs. S15-S16).

D. Fluctuation spectrum: Figure S7 (and Fig. 3A) plots typical experimental spectrum of the membrane fluctuations obtained for the two vesicle classes. Similar results were

obtained for different vesicles in a population of 20 different specimens taken from several synthesis batches.

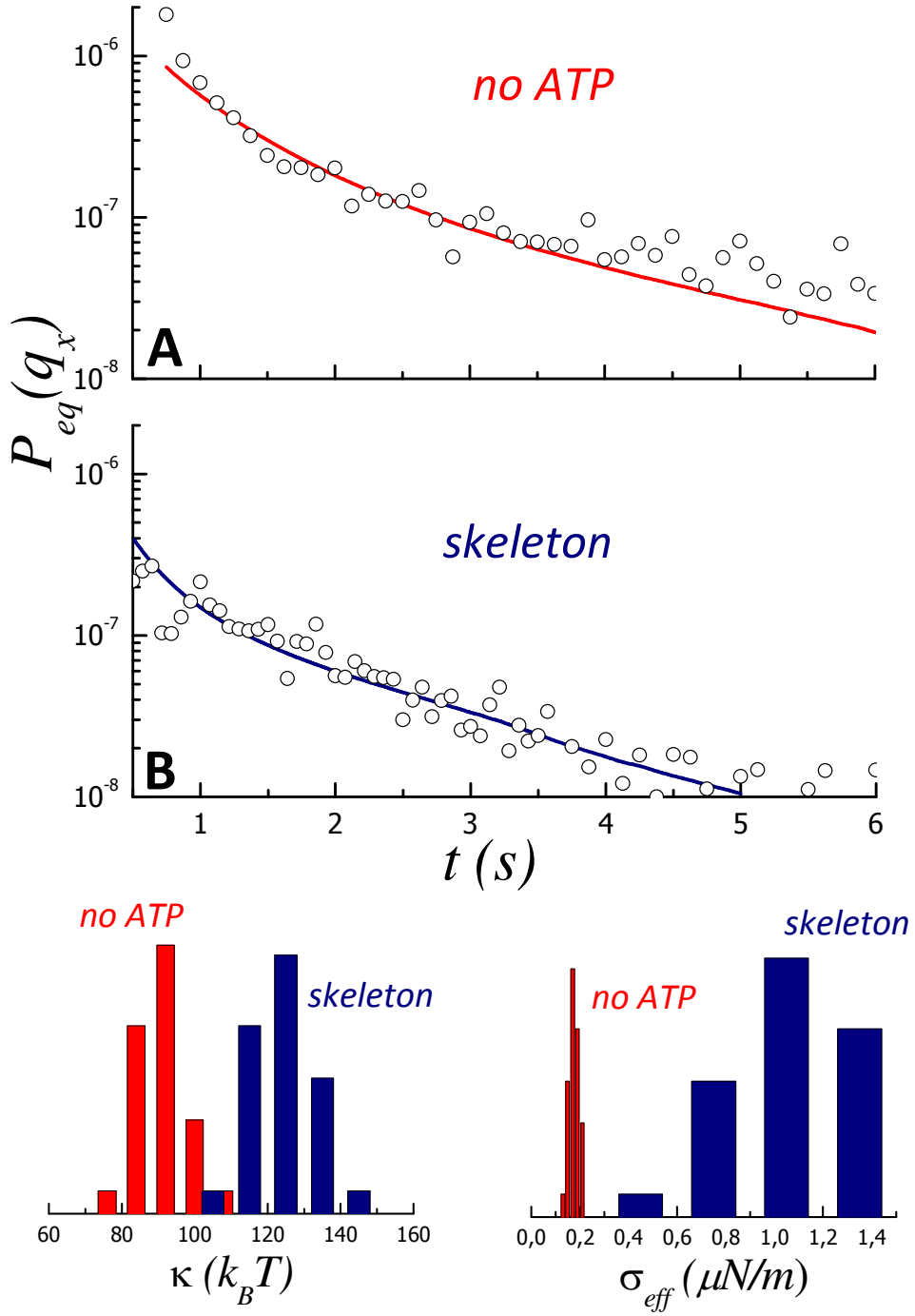

Figure S7. Experimental spectra of the membrane fluctuations of erythGUV's: A) in the absence of ATP and B) in the presence of ATP (2 mM) an subsequent skeleton formation. The lines represent the best fit to the equatorial projection of the Helfrich spectrum (Eq.S10). The statistics in the bottom panel corresponds to the fitting parameters (*left:* bending modulus κ; *right:* effective tension σ_{eff} as defined in Eqs. S15-S16) obtained over vesicles populations ($N = 20$).

Following Pécrèaux's schema, data are fitted to Eq. S10 and the parameters obtained for each vesicle. After statistics (see histograms in Fig. S7), we obtain: κ_0 = 90 (±5) k_BT, σ_0 = 0.17 (±0.02) μN/m for the bare vesicles and κ_{sk} = 120 (±11) k_BT, σ_{sk} = 1.1 (±0.2) μN/m when skeleton is formed (quantities between parentheses correspond to standard deviations; N = 20). From Eq. S16, we estimate a value μ = 400 (±200) μN/m for the shear modulus of the artificial skeleton. The shear modulus has been experimentally measured for the native red cell cytoskeleton. Using micropipetes[22-25] , optical tweezers[26, 27] and flickering spectroscopy[28], different authors coincide to assign a value $\mu_{nat} \approx 6\mu$N/m. Higher values (in the range $\mu_{nat} \approx 13\text{-}22\mu$N/m) were earlier reported from red cell stretching experiments performed under optical traps[29]. From the experimental value, μ ≈400 μN/m, the quadratic shear-regime described by Eq.S13 is expected at wavevectors above $q_C \approx 0.4\mu m^{-1}$, close to the lowest spherical harmonic possible in a typical vesicle ($R \approx 10$ μm), $q_{low} \approx 2/R \approx 0.2\ \mu m^{-1}$. This stimation confirms the validity of the approximated spectrum in Eqs. S15-S16.

The high value of the shear modulus estimated from experiments, $\mu_{art} \approx 10^2\mu$N/m, (practically two order of magnitude larger than the value measured for the native spectrin cytoskeleton) assigns a higher intrinsic rigidity to the reconstituted macroscopic filaments with respect to the elemental spectrin tetramers (SpT) constituting the original cytoskeleton network. This difference suggests a larger persistence length for the macroscopic bundles than for elemental spectrin filaments. This points to actin as the filament component responsible for such a reinforced stiffness. From a structural standpoint, actin filamentsare known to show a high conformational persistence ($l_p \approx 2\mu$m)[30], producing very rigid structures able to impinge marked structural stiffening to the topological network where they are embedded[31]. On the opposite side, spectrin units fold into triple helical coiled-coils ($R_g \approx$ 20-30nm) compatible with a low intrinsic rigidity dominated by entropic elasticity[32]. Single molecule nanomechanical studies performed by AFM dynamometry confirm the picture, revealing indeed a shallow unfolding potential[33]. This confirms an entropic origin for the shear elasticity of native spectrin networks, $\mu \approx k_{sp}$ [34]. For entropic coils the spring constant takes a value of the order of $k_{sp} \approx k_BT/R_g^2 \approx 10$ μN/m, in qualitative agreement with mechanical experiments, thus $\mu_{nat} \approx$ 6-20 μN/m, in agreement with mechanical experiments[22-28].

Because shear stiffness causes effective tension to increase (Eq. S16), and conversely, higher lateral tension induces higher shear rigidity, $\mu \approx (\sqrt{3}k_{sp}/4)\cdot(1+\sqrt{3}\sigma/k_{sp})$ (***Error!***

Bookmark not defined.), the presence of the rigid skeleton is expected to principally cause lateral structural stiffening detected as a significant increase of the effective lateral tension. In flickering experiments, this effect might appear visible as a dominance of the capillary regime in the equatorial fluctuation spectra, $P_{sk}(q) \approx k_BT/\sigma^{(eff)}q$, as experimentally observed (see Fig. 3A).

E. Autocorrelation function. The amplitude autocorrelation functions $G(t) = <\zeta_q(0)\ \zeta_q(t)>$ are numerically calculated over sequences of 5000 frames, typically, using a MATLAB code. To minimize the pixelization noise, the dynamical analysis was restricted to the first modes ($l < 12$); here, the smallest resolved distance is of the order of $q^{-1}_{max} \approx 1\mu m$ ($l_{max} = 12$), well above the pixel size (0.1 μm). The normalised autocorrelation functions match a stretched-exponential profile as:

$$G(t) \sim \exp\left[-\left(\Gamma_q t\right)^{\beta}\right] \qquad \text{Eq. S17}$$

characterised by a stretching exponent $0.5 < \beta < 1.0$, typical of rigid membranes[13, 35] and the q-dependent relaxation rate of the tension-bending modes[36]:

$$\Gamma_q = \frac{\sigma q + \kappa q^3}{4\eta} \qquad \text{Eq. S18}$$

where the numerator defines the elastic response of the membrane (σ is the surface tension and κ the bending modulus; in the presence of rigid skeleton, the effective tension, $\sigma_{sk} = \sigma^{(eff)}$, is dependent on the shear modulus as given in Eq. S16). The denominator accounts for the viscous dissipation imposed by bulk friction (η is the bulk viscosity of the solvent).

Using time-resolved experimental data, from the time series of the Fourier amplitudes $\zeta_q(t)$, one calculates the normalized autocorrelation functions as:

$$G_q(t) = \left\langle z_q(0) z_q(t) \right\rangle \qquad \text{Eq. S19}$$

Figure S8 plots the experimental autocorrelation functions obtained for different fluctuation modes in a given vesicle. Meaningfully, a clear increase of the relaxation rates is observed upon skeleton formation after ATP addition. This acceleration has been attributed to the mechanical stiffening imposed by the spectrin skeleton, which represents a solid-like topological network with a finite shear rigidity and a lateral tension much higher than the bare lipid bilayer (which is intrinsically fluid). Similar results were obtained for the different vesicles in same population as in Section D.

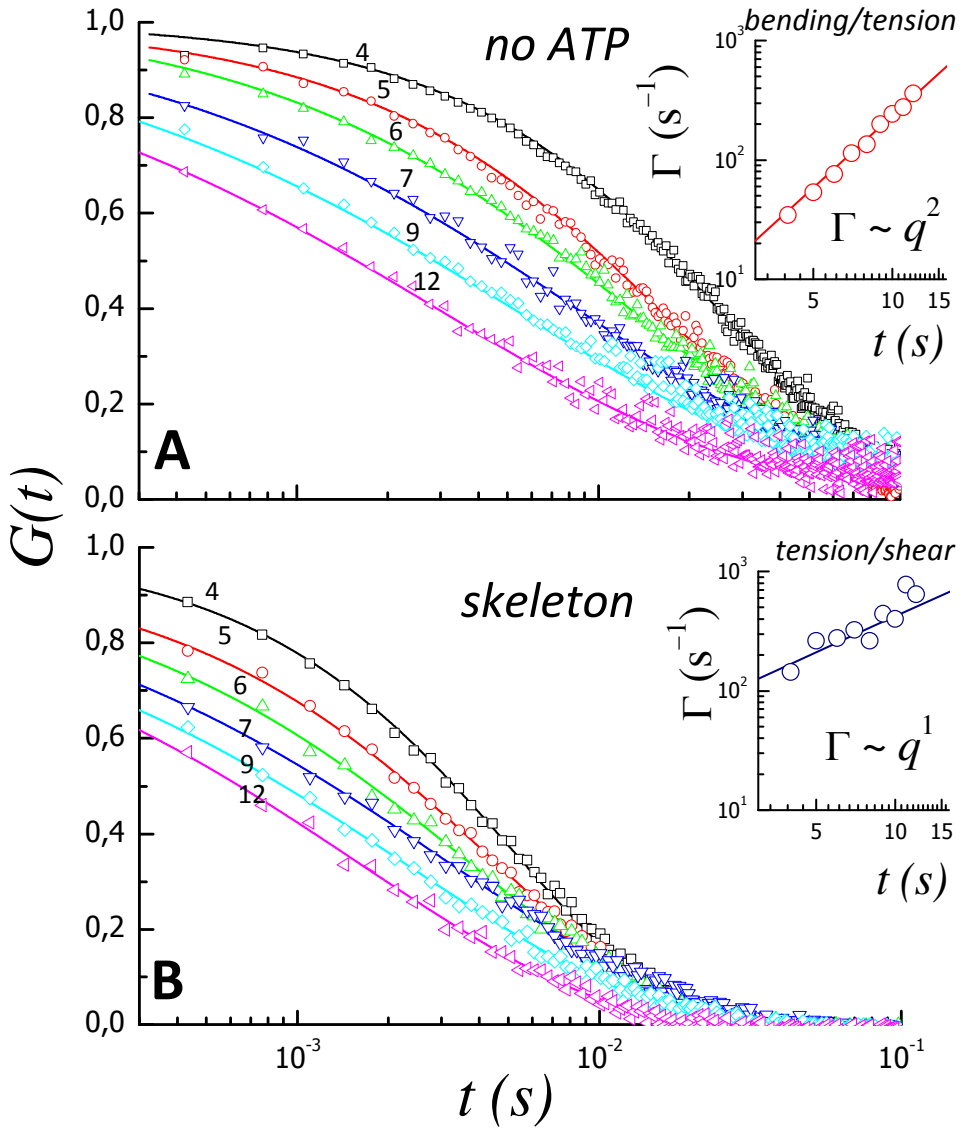

Figure S8. Experimental autocorrelation functions obtained for erythGUV's: ***A)*** in the the absence of ATP and ***B)*** in the presence of ATP (1mM) an subsequent skeleton formation. The numbers indicate the fluctuation mode (l; $q = l/R$). The lines represent the best fits to Eq. S18.

The analysis of the experimental autocorrelation functions in terms of Eqs. S17-18 allows for a quantitative determination of the relaxation rates Γ_q. From the dispersion plots (see insets in Fig. S8), the numerical values of the mechanical parameters can be obtained by fitting to Eq. S18. The equivalent data in the inset of Fig. 3B (main text) correspond to a statistical average over the 20 different vesicles considered in this study (the error bars represent a standard deviation). After statistics, the average relaxation frequencies are found compatible with the mechanical parameters calculated from the

static spectra (the straight lines in the inset of Fig. 3B correspond the predictions from Eq. S18 for the values of σ_{eff} and κ found in Section D).

REFERENCES

(1) Steck, T. L.; Kant, J. A., Preparation of impermeable ghosts and inside-out vesicles from human erythrocyte membranes. *Methods Enzymol* **1974,** 31, (Pt A), 172-80.

(2) Burton, G. W.; Ingold, K. U.; Thompson, K. E., An improved procedure for the isolation of ghost membranes from human red blood cells. *Lipids* **1981,** 16, (12), 946.

(3) Weber, K.; Osborn, M., The reliability of molecular weight determinations by dodecyl sulfate-polyacrylamide gel electrophoresis. *J. Biol. Chem* **1969,** 244, (16), 4406-12.

(4) Song, C.; Havlin, S.; Makse, H. A., Self-similarity of complex networks. *Nature* **2005,** 433, (7024), 392-395.

(5) Spanier, E. H., *Algebraic topology*. Springer Verlag: 1994; Vol. 55.

(6) Buño, I.; Juarranz, A.; Cañete, M.; Villanueva, A.; Gosalvez, J.; Stockert, J. C., Image processing and analysis of fluorescent labelled cytoskeleton. *Micron* **1998,** 29, (6), 445-449.

(7) Pratt, W. K., *Digital image processing*. Wiley-Interscience 2 edition 1991; p 720.

(8) Tolle, C. R.; McJunkin, T. R.; Gorsich, D. J., An efficient implementation of the gliding box lacunarity algorithm. *Phys D* **2008,** 237, (3), 306-315.

(9) Hamida, T.; Babadagli, T., Fluid-fluid interaction during miscible and immiscible displacement under ultrasonic waves. *EPJB* **2007,** 60, (4), 447-462.

(10) Vadakkan, T., http://www.mathworks.com/matlabcentral/fileexchange/25261. **2009**.

(11) Tolle, C. R.; McJunkin, T. R.; Rohrbaugh, D. T.; LaViolette, R. A., Lacunarity definition for ramified data sets based on optimal cover. *Phys D* **2003,** 179, (3-4), 129-152.

(12) De Gennes, P., *The Physics of Liquld Crystals*. Clarendon Press, Oxford: 1995.

(13) Rodríguez-García, R.; Mell, M.; López-Montero, I.; Monroy, F., Subdiffusive fluctuation dynamics of rigid membranes as resolved by ultrafast videomicroscopy. *EPL* **2011,** 94, (2), 28009.

(14) Pecreaux, J.; Dobereiner, H. G.; Prost, J.; Joanny, J. F.; Bassereau, P., Refined contour analysis of giant unilamellar vesicles. *EPJE* **2004,** 13, (3), 277-90.

(15) Rodríguez-García, R.; Arriaga, L.; Mell, M.; Moleiro, L.; López-Montero, I.; Monroy, F., Bimodal Spectrum for the Curvature Fluctuations of Bilayer Vesicles: Pure Bending plus Hybrid Curvature-Dilation Modes. *Phys. Rev. Lett.* **2009,** 102, (12), 128101.

(16) Helfrich, W., Elastic properties of lipid bilayers: theory and possible experiments. *Z. naturforsch* **1973,** 28, (11), 693-703.

(17) Aronovitz, J.; Golubovic, L.; Lubensky, T., Fluctuations and lower critical dimensions of crystalline membranes. *J.Phys* **1989,** 50, (6), 609-631.

(18) Nelson, D. R., *Defects and geometry in condensed matter physics*. Cambridge Univ Pr: 2002.

(19) Lipowsky, R.; Girardet, M., Shape fluctuations of polymerized or solidlike membranes. *Phys. Rev. Lett.* **1990,** 65, (23), 2893-2896.

(20) Peterson, M. A.; Strey, H.; Sackmann, E., Theoretical and phase contrast microscopic eigenmode analysis of erythrocyte flicker: amplitudes. *J.Phy2* **1992,** 2, (5), 1273-1285.
(21) Auth, T.; Safran, S. A.; Gov, N. S., Fluctuations of coupled fluid and solid membranes with application to red blood cells. *Phys. Rev. E* **2007,** 76, (5 Pt 1), 051910.
(22) Evans, E. A., Bending elastic modulus of red blood cell membrane derived from buckling instability in micropipet aspiration tests. *Biophys. J.* **1983,** 43, (1), 27-30.
(23) Evans, E.; Yeung, A., Hidden Dynamics in Rapid Changes of Bilayer Shape. *CPLip* **1994,** 73, (1-2), 39-56.
(24) Discher, D.; Mohandas, N.; Evans, E., Molecular maps of red cell deformation: hidden elasticity and in situ connectivity. *Science* **1994,** 266, (5187), 1032.
(25) Hochmuth, R. M., Micropipette aspiration of living cells. *J.Biom* **2000,** 33, (1), 15-22.
(26) Li, Y.; Wen, C.; Xie, H.; Ye, A.; Yin, Y., Mechanical property analysis of stored red blood cell using optical tweezers. *Colloids Surf. B. Biointerfaces* **2009,** 70, (2), 169-173.
(27) Lewalle, A.; Parker, K. H., Axisymmetric Optical-Trap Measurement of Red Blood Cell Membrane Elasticity. *J Biomech* Eng **2011,** 133, (1), 011007.
(28) Park, Y.; Best, C. A.; Badizadegan, K.; Dasari, R. R.; Feld, M. S.; Kuriabova, T.; Henle, M. L.; Levine, A. J.; Popescu, G., Measurement of red blood cell mechanics during morphological changes. *Proc. Natl. Acad. Sci. USA p* **2010,** 107, (15), 6731-6736.
(29) Dao, M.; Lim, C.; Suresh, S., Mechanics of the human red blood cell deformed by optical tweezers. *J Mech Phys Solids* **2003,** 51, (11-12), 2259-2280.
(30) Kaufmann, S.; Käs, J.; Goldmann, W.; Sackmann, E.; Isenberg, G., Talin anchors and nucleates actin filaments at lipid membranes A direct demonstration. *FEBS Lett.* **1992,** 314, (2), 203-205.
(31) Gardel, M. L.; Shin, J. H.; MacKintosh, F. C.; Mahadevan, L.; Matsudaira, P.; Weitz, D. A., Elastic Behavior of Cross-Linked and Bundled Actin Networks. *Science* **2004,** 304, (5675), 1301-1305.
(32) Sotomayor, M.; Schulten, K., Single-molecule experiments in vitro and in silico. *Science* **2007,** 316, (5828), 1144.
(33) Rief, M.; Pascual, J.; Saraste, M.; Gaub, H. E., Single molecule force spectroscopy of spectrin repeats: low unfolding forces in helix bundles1. *J.M.Bio* **1999,** 286, (2), 553-561.
(34) Boal, D. H., *Mechanics of the Cell*. Cambridge Univ Pr: 2002.
(35) Zilman, A. G.; Granek, R., Undulations and Dynamic Structure Factor of Membranes. *Phys. Rev. Lett.* **1996,** 77, (23), 4788-4791.
(36) Milner, S. T.; Safran, S. A., Dynamical fluctuations of droplet microemulsions and vesicles. *Phys.Rev.A* **1987,** 36, (9), 4371-4379.